Applicability of superelastic materials in seismic protection systems: a parametric study of performance in isolation of structures

2017 Smart Mater. Struct. 26 085036

(http://iopscience.iop.org/0964-1726/26/8/085036)

IOP Publishing Smart Materials and Structures
Smart Mater. Struct. **26** (2017) 085036 (16pp) https://doi.org/10.1088/1361-665X/aa7caf

Applicability of superelastic materials in seismic protection systems: a parametric study of performance in isolation of structures

H Soul[1] **and A Yawny**[1,2]

[1] CONICET, Division Metales, Centro Atómico Bariloche (CNEA), Instituto Balseiro (UNCuyo), Bustillo 9500, (8400) San Carlos de Bariloche, Argentina
[2] CNEA, División Metales, Centro Atómico Bariloche (CNEA), Instituto Balseiro (UNCuyo) Bustillo 9500, (8400) San Carlos de Bariloche, Argentina

E-mail: hugo.soul@gmail.com

Received 11 January 2017, revised 23 June 2017
Accepted for publication 30 June 2017
Published 24 July 2017

Abstract

The dynamic response to different seismic inputs of an isolated structure disposed on a sliding layer and connected to the ground with a superelastic NiTi device was analyzed. The device allows wires of NiTi to be mechanically cycled by supporting externally applied tension/compression forces exploiting both dissipative and self-centering capabilities associated with superelasticity. Simulations were carried out modifying the wires length and the structural mass. Both parameters were varied over two orders of magnitude with the aim of evaluating the type of response, the mitigation level that can be accomplished and the combination of parameters resulting in an optimal response. Results indicate that the proposed device is suitable for seismic protection of isolated structures and it is demonstrated that the protective action is more related with the restraining and self-centering properties of the NiTi superelastic wires than with its damping capacity.

Keywords: superelastic device, dynamical response, performance analysis

(Some figures may appear in colour only in the online journal)

1. Introduction

Superelastic effect is the behavior exhibited by the so-called shape memory alloys (SMA) by which a reversible solid-to-solid phase martensitic transformation is induced upon mechanical loading. Once a critical stress level is reached, the SMA transforms from a phase referred to as austenite to a phase referred to as martensite developing strains up to 8% (Otsuka and Wayman 1998). Upon unloading, nearly full recovery of the original dimensions occurs with the reverse transformation taking place at a stress level lower than the one for the forward transformation (Miyazaki *et al* 1981). The basic superelastic effect is illustrated in figure 1. This stress difference between the forward and reverse transformations represents a mechanical hysteresis and the area enclosed in the resulting stress-strain response indicates that energy is dissipated in the process. In addition, the existence of a stress level associated with the reverse transformation and the high efficiency of the strain recovery on SMA provides the protected structures with self-centering capabilities (Cardone 2012). These characteristics of the superelastic behavior makes SMA potential candidates for the construction of devices aimed to increase the resistance of structures subjected to seismic loads (Graesser and Cozzarelli 1991, Saadat *et al* 2002, Wilson *et al* 2005). This constitutes a significant difference with respect to dissipative devices based on the plastic deformation of conventional metallic materials. In the present work, the interest is focused on devices whose working principle is based on the energy dissipation and the self-centering force associated with the superelastic effect.

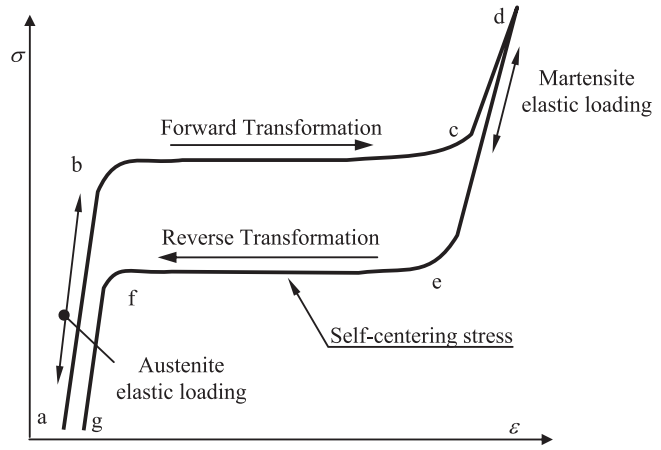

Figure 1. Schematic of a superelastic cycle indicating the main functional parameters.

Such a device will be referred to as Superelastic Device (SED) in what follows.

The effects of incorporating a SED to a structure subjected to seismic action are now briefly considered. Under small load excitations the shape memory superelastic material would behave as a standard elastic material, i.e., with the stiffness proper of the austenitic phase (figure 1, path a–b). Once load reaches a critical level, the material will transform at rather constant stress from austenite to martensite (figure 1, path b–c). The appearance of the stress induced transformation, on the one hand, sets a limit to the magnitude of the load transferred to the structure and, on the other hand, results in energy dissipation. In the case of higher shaking intensity, the displacements associated with the transformation will be exhausted. The SMA material would then again exhibit a high stiffness response, now associated with the elastic behavior of the martensite (figure 1, path c–d) and this will favor avoiding structural collapse (Biritignolo *et al* 2000). When reverting the displacement direction, the force will first decrease in martensite (figure 1, path d–e) until the critical stress for retransformation is reached. A nearly constant force will be applied on the structure upon further reversion (figure 1, path e–f). Finally, the force will decrease according to the stiffness of the austenite phase (figure 1, path f–g).

Numerous research works were devoted to the characterization and improvement of the mechanical and functional properties of superelastic materials (Chen *et al* 2009, Tanaka *et al* 2010) as well as pursuing their efficient implementation as kernel elements in different damping device concepts (Torra *et al* 2009, Dell Ville *et al* 2010). In recently published articles (Torra *et al* 2016, 2017), deviations from the ideal superelastic behavior described above are considered. These authors refer to *s-shaped* superelastic behavior to describe the mechanical response exhibited by certain types of NiTi wires, (diameter above a certain value). These authors attribute and increased dissipative capacity associated with the s-shaped hysteresis cycle which would favor their use in environments with high temperature variations. Another important aspect that concerns current interest is the fatigue life properties of superelastic wires, since this implies a limiting factor in almost all technological applications. Fatigue life characterization and modeling under superelastic loading (Casciati *et al* 2017) and analysis of the effect of the shape, size and distribution of inclusions in the fatigue resistance (Launey *et al* 2014, Ulmer *et al* 2015) can be enumerated among the most recent contributions.

Other works described particular devices able to exploit superelasticity for structural control in tensile (Terriault *et al* 2007), bending (Dolce and Cardone 2005, Casciati *et al* 2007) or torsion (Han *et al* 2005, Mirzaeifar *et al* 2010) configurations. Although different geometries for the kernel elements were employed, including bars (Des Roches and Delemond 2002), tension-compression springs (Attanasi and Auricchio 2011), Belleville washers (Speicher *et al* 2009), rings (Gao *et al* 2016), the use of wires was by far the most considered. The very recent development of NiTi SMA cables (Reedlunn *et al* 2013) would represent an interesting alternative for future developments. The extended use of NiTi wires can be understood in terms of the vey mature technologies for their manufacturing (Ozbulut *et al* 2011). The intense use of the wire geometry subjected to uniaxial loadings is also related with the high material usage efficiency in terms of load per unit mass.

The implementation of a structure protection system based on the damping properties associated with the superelastic effect requires however more in depth considerations. Firstly, it has to be noticed that, for a given seismic excitation, the dynamical response of a protected structure will be modified by the presence of the particular SED adopted. In effect, the magnitude of the forces exerted by the SED on the structure will be determined by the total transverse area sections A of the SMA kernel elements employed. The maximum recoverable extensions, i.e., the SED stroke, will in turn depend on the active length L of the SMA elements. Thus, both SMA kernel transverse area A and length L will contribute to the overall stiffness of the system and, together with the effective mass M of the system, will also influence the eigenfrequency of the structure. By modifying A and L, the dynamic response will range from that corresponding to a fully stiffened system (high A and short L) to the one characteristic of an unprotected system (small A and long L). An efficient implementation would then require assessing the attainable performance level for all possible device configurations in order to select the most convenient combination of parameters. The objective function behind an optimum design will be specific of the studied structure and would include appropriate weighing factors for the minimization of peak absolute acceleration levels, the maximum relative displacement and the residual displacement after the Earthquake.

The studies concerning an efficient implementation of SED available in the literature have focused on evaluating the effects on the dynamic response of the functional parameters associated with the superelastic behavior; i.e., the transformation stresses, the mechanical hysteresis and the slope of the stress induced transformation. By proceeding in this manner however, only aspects related with the superleastic material itself could be analyzed. Among this kind of studies, Attanasi *et al* (2009) analyzed the feasibility of using superelastic

materials in structures´ base isolation by comparing their performance with lead rubber based devices. Cardone (2012) studied the response of simple structures equipped with superelastic materials focusing on the effect of parameters defining the behavior on the residual displacement. Similarly, Ling and Ling (2012) investigated the effect of pre/post yielding stiffness ratios on the performance of SEDs with self-centering and dissipating modules. Ozbulut and Silwal (2016), considered a 3 storey—4 bay benchmark frame building equipped with combined novel friction and superelastic NiTi cables devices. Using a genetic algorithm, they studied the optimization of the response considering as variable parameters the friction coefficient, the superelastic yielding force and the displacement. Masuda and Noori (Masuda and Noori 2002) have studied the influence of the shape of a superelastic cycle in the response of a protected structure under harmonic excitations.

In the present work, the problem is analyzed from a different perspective. This is done by performing numerical simulations to systematically study the dynamic response of an idealized structure consisting in a mass M lying on a PTFE friction layer and linked to the ground through the tension-compression SED characterized in a previous article (Soul and Yawny 2015). The SED kernel consists in a parallel arrangement of two NiTi wires of length L and diameter $d = 1.2$ mm. For the simulations, it is assumed that the superelastic behavior does not depend on frequency and it can be scaled to any wire length. Both parameters have been varied along two orders of magnitudes, i.e., L from 0.08 to 8 m and M from 20 to 2000 kg. Five different seismic inputs compatible with the Argentinean most hazardous zones according to the Argentinean Seismic Risk Prevention Institute INPRES (2013) have been considered for the analysis. The possible responses accomplished by the structure—device system are addressed, focusing on maximum absolute accelerations, maximum relative displacement of the isolated mass and maximum strains in the wires. It is evaluated whether there is an M/L parameter combination which effectively optimizes the protective action of the SED. The efficiency of the device is assessed, firstly, by analyzing the ratio between the energy dissipated by the superelastic effect and the total inputted energy provided by the seismic excitation. Then the responses obtained for the selected M/L configuration are compared with the ones corresponding to the unprotected system and also with the responses obtained with a fully elastic device whose stiffness is set equivalent to that of the SED.

2. Isolated structure on PTFE layers

The concept of seismic isolation is based upon the existence of a cut plane between the structure and the ground subjected to the Earthquake excitation. In an ideal situation, this interface would be frictionless and no shear forces would be transmitted. In actual devices however, a friction force between a PTFE layer and the structure exists (Kelly 2001). This force represents a shear stress threshold for the relative movement between the ground and the structure to take place. On the one hand, this threshold stress inhibits relative displacements that might be originated in low intensity loads such as those caused by wind or weak seismic activity. On the other hand, it sets a limit for the maximum load transferred to the structure in case of demanding ground shaking. Such type of isolated structures however, develops high displacements with the consequent risk of damage of the internal facilities, out setting from bearings, or damage due to impacts with the neighbor buildings (Chopra 1985). In this context, the use of SEDs in combination with a sliding bearing system might constitute a convenient alternative, providing additional protective dissipative and self-centering capabilities. This is precisely the object of study of the present work where a structure linked to the ground with a SED in the way schematically illustrated in figure 2 is considered. In the context of the present work, the structure is modeled as a one degree of freedom (1 DOF) system consisting in a monolithic mass M

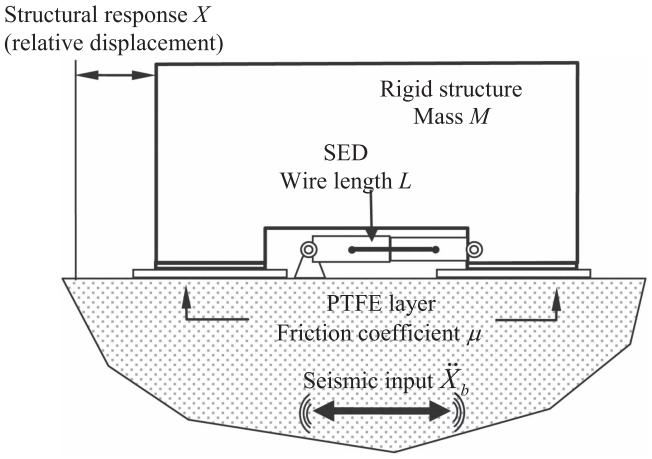

Figure 2. Schematic representation of the studied structure consisting in a rigid mass M sliding over a PTFE layer. The superelastic device SED is inserted as a restrainer which links the mass with the ground.

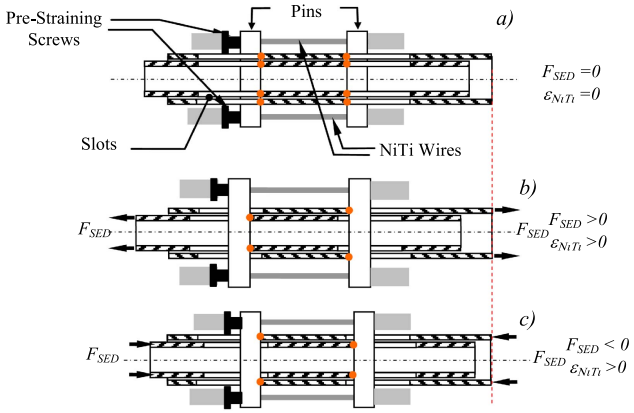

Figure 3. Schematic explanation of the SED working principle (external tube position fixed, indicated by the vertical red dashed line at the right of the figure). (a) Initial condition upon mounting, no external load; each pin is in contact simultaneously with both tubes. Relative displacement of the tubes moves the pins which in turn produces the straining of the NiTi wires. The wires are subjected to tension whenever the external force is positive (b) or negative (c), respectively.

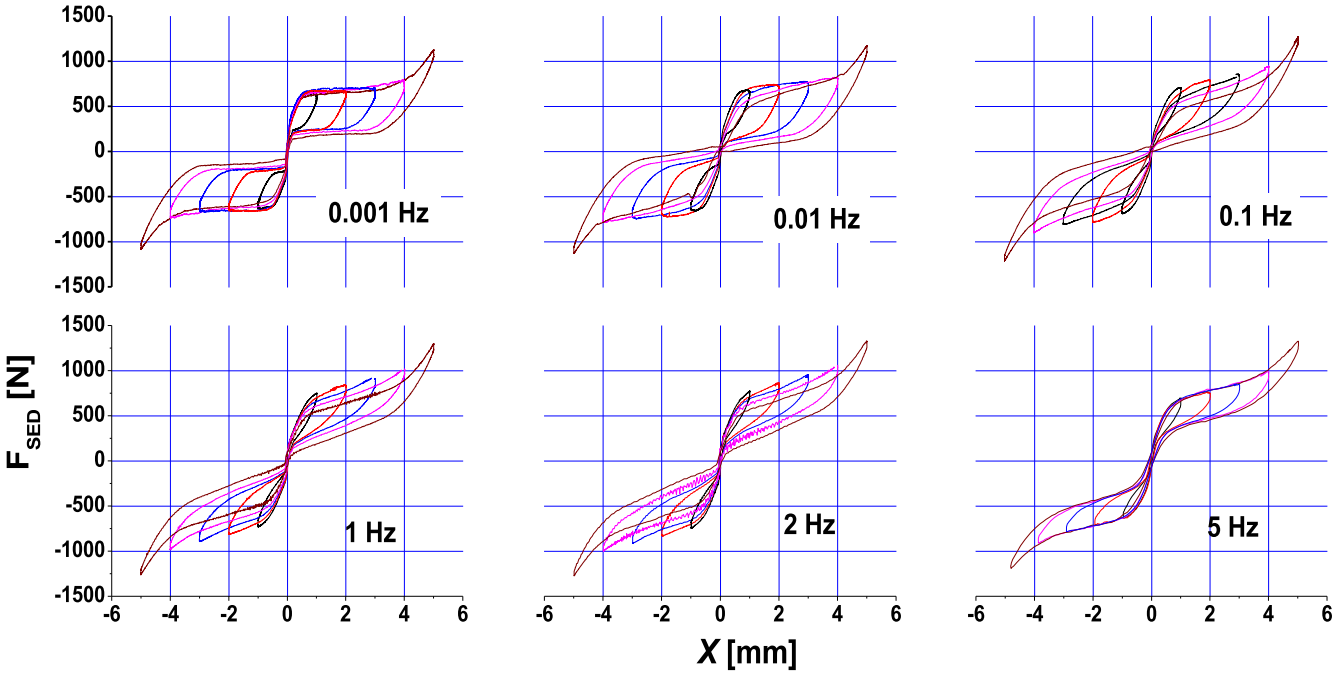

Figure 4. Summary of the F_{SED}–X results for six of the twelve tested frequencies for the SED. The individual curves represent the device response corresponding to the first cycle for each combination of frequency and displacement amplitude considered. The different colored curves correspond to the different amplitudes of 1, 2, 3, 4 and 5 mm imposed on the tests (Soul and Yawny 2015).

sliding rigidly over a PTFE isolation layer with a friction coefficient $\mu = 0.04$ (Erot 2007) which provides a friction shear force of magnitude $F_{fric} = \mu\ M\ g$, opposing the relative movement.

3. Superelastic damping device

Figure 3 schematizes the SED considered in the present study. The working principle and an experimental characterization of a prototype have been presented in detail elsewhere (Soul and Yawny 2015) and are briefly reviewed in what follows. The SED consists of two coaxial steel tubes, one sliding (frictionless) inside the other. Both tubes are crossed by two pins in the transversal direction through longitudinal machined slots. Two superelastic NiTi wires are extended between the pins, one at each side of the tubes. The initial condition of the device, free of external loads, is illustrated in figure 3(a). Dots are included in the drawings in figures 3(a)–(c) to denote the contact points between the pins and the slots along a complete working cycle. When tubes slide, slots bearings push against the pins that in turn stretch the wires either for tensile or compressive forces. By introducing superelastic NiTi wires it is possible to obtain the characteristic double flag force versus displacement behavior, F_{SED}–X (subindex SED designates the force exerted by the SED on the structure), which indicates dissipative and self-centering capabilities (Cardone 2012). The previous experimental characterization (Soul and Yawny 2015) also indicated that the introduction of a certain wire pre-strain, allowed the compensation of permanent plastic strains introduced during cycling thus keeping the wires always tight. The SED prototype was equipped with two NiTi wires of diameter $d = 1.2$ mm and length $L = 80$ mm.

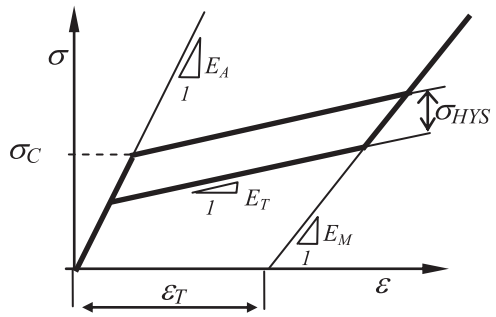

Figure 5. Multilinear model describing the superleastic effect in NiTi SMA.

Figure 4 shows the F_{SED}–X diagrams obtained for experimental tests performed at different frequencies in the range from 0.001 to 5 Hz. An important effect of the cycling frequency on the shape of the superelastic curves was observed during the experiments. This dependence is mainly due to the temperature changes provoked by the latent heat of transformation associated with the martensitic transformation and the coupling between transformation stresses and temperatures, subjects that were broadly studied in NiTi alloys (see for example Soul and Yawny 2013 and references herein).

4. Modeling of the superelastic behavior

In the present work, a simplified model is assumed to describe the NiTi wire superelastic behavior which in turn determines the SED mechanical response. The model states that a complete superelastic cycle is defined by the six parameters illustrated in figure 5, i.e., the critical stress σ_C; the transformation strain ε_T, the austenitic and martensitic elastic modulus, E_A and E_M; the

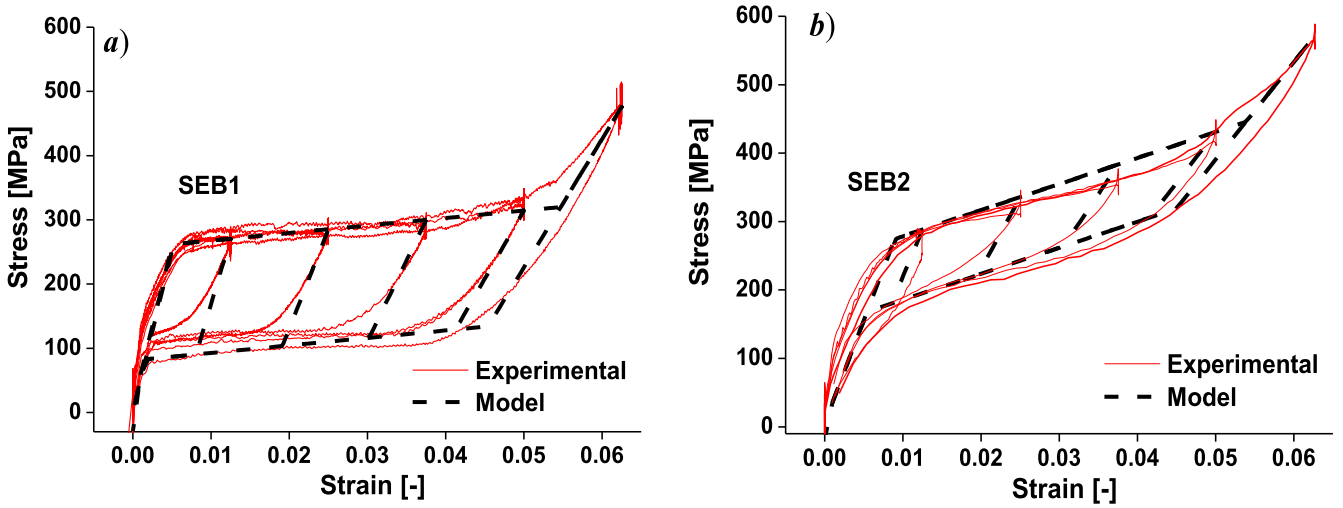

Figure 6. Superelastic stress-strain curves obtained with the multilinear model compared with their experimental counterparts. (a) Set of parameters SEB1 from table 1. (b) Set of parameters SEB2 from table 1.

Table 1. Model parameters.

	SEB1	SEB2
E_A (GPa)	50	30
E_M (GPa)	20	14.25
E_T (GPa)	1.17	3.8
σ_C (MPa)	262	275
σ_{HYS} (MPa)	175	93
ε_T (-)	0.039	0.023

slope of the stress induced transformation E_T and the hysteresis width σ_{HYS}. The parameters corresponding to the behavior of a superelastic material are evaluated by adjusting a cycle obtained experimentally with linear segments. Since this model does not account for the frequency or rate dependence of the superelastic behavior, the parameters set should be associated with the corresponding experimental condition. For the analysis performed in this work, two different model parameters sets were utilized: SEB1 and SEB2, extracted from experimental cycles of the mentioned SED prototype, presented in figure 5 and corresponding to the two extremes frequencies of 0.001 and 5 Hz, respectively. It is worth to mention that both experiments were performed at the same room temperature, around 22 °C and still air. The parameters, summarized in table 1, were obtained by normalizing the force and the displacement by the two wires cross section area and the wire length L, respectively. In figure 6 the normalized stress versus strain curves (experimental) for both frequencies are represented together with the mechanical response associated with the simplified model in each case.

The adjusted σ–ε cycles are scaled for any selected wire length for describing the double flag F_{SED}–X curves corresponding to the SED behavior. In figure 7(a), the F_{SED}–X behavior obtained with wire lengths L and $2L$ is schematized. The influence of the mass M can be appreciated when the combined action of the SED and the PTFE is considered (figure 7(b)) for the values M and $2M$. These two schematic figures help understanding the influence of both L and M parameters on the whole system behavior. A long wire results in a less stiff behavior and provides a more extended displacement associated with the transformation plateau. An increase in the mass M results in a decrease of the self-centering capacity of the SED together with a lower significance of the SED damping capacity on the overall behavior.

5. Equation of motion and dissipated energies

The forces acting on the mass M structure are the force exerted by the SED, F_{SDE}, the force due to friction, F_{fric}, and a viscous type or force representing different interactions proportional to the relative speed of motion respect to ground, F_{vis}. As explained before, the combined effect of SED and friction is given by the force $F = F_{SED} + F_{fric}$ represented in figure 7(b) right. The equation of motion of the mass M described from an external inertial reference system can be expressed as:

$$F_{SED} + F_{fric} + F_{vis} = M\ddot{X}_{abs}, \tag{1}$$

where $\ddot{X}_{abs}$ is the absolute acceleration given by the sum of the ground plus the relative acceleration:

$$\ddot{X}_{abs} = \ddot{X}_b + \ddot{X}. \tag{2}$$

The force due to friction can be expressed as:

$$F_{fric} = -\mu g M \ \mathrm{sgn}(\dot{X}), \tag{3}$$

while that due viscous force, proportional to the relative velocity, can be expressed as:

$$F_{vis} = -C\dot{X}. \tag{4}$$

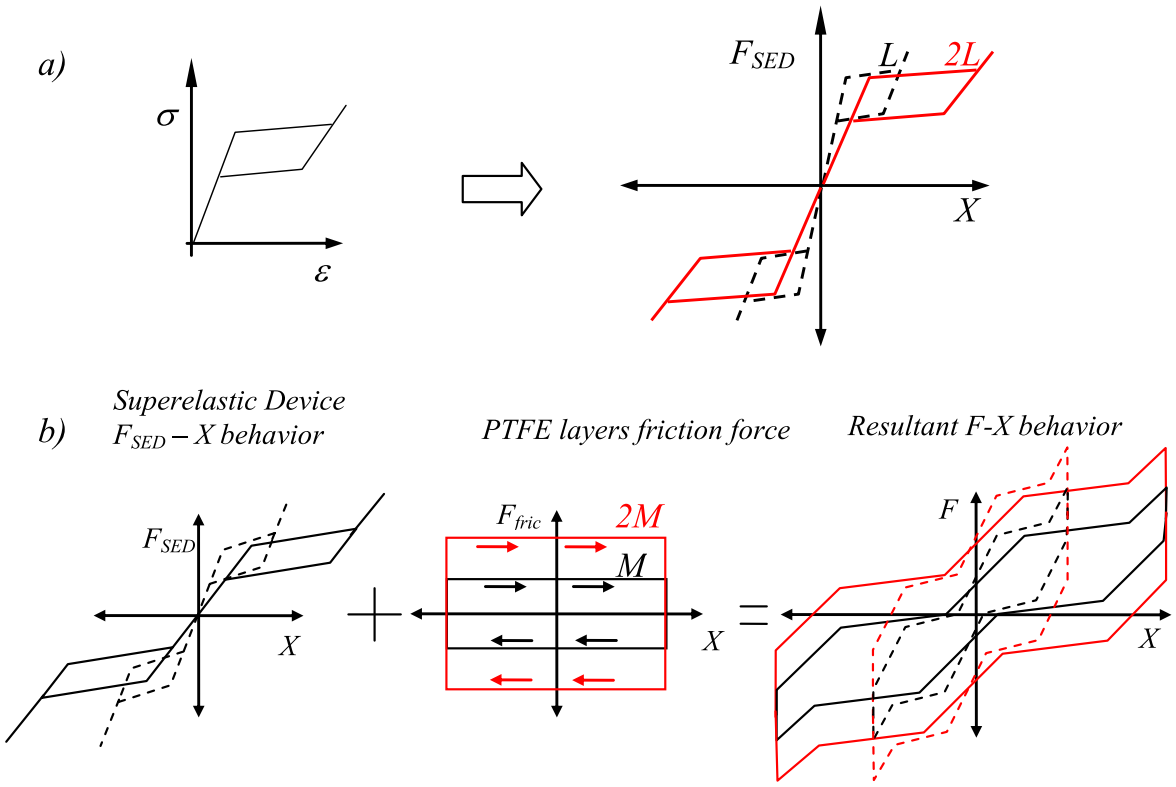

Figure 7. (a) F_{SED}–X behavior of the SED with different wire lengths with a given σ–ε superelastic cycle. (b) Resultant F–X behavior of the whole system obtained by the addition of the contributions of the SED and PTFE layer friction, showing the effect of doubling the wire length L and/or the associated mass M.

Then, substituting (2)–(4) in (1), reordering and dividing by the mass M, the equation of motion in terms of the relative displacement X can be expressed as:

$$\ddot{X} + \frac{C}{M}\dot{X} + \mu g\ \mathrm{sgn}(\dot{X}) - \frac{F_{\mathrm{SED}}}{M} = -\ddot{X}_b. \tag{5}$$

Inspection of equation (5) shows that the higher the mass the lower the influence of superelastic and viscous forces on the movement will be. Along with the calculation of position and force, the different work inputs and energies are evaluated. The work input to the structure per mass unit w_{in} at any instant t is obtained by integrating the external action as:

$$w_{\mathrm{in}} = \int_0^t -\ddot{X}_b \dot{X}\mathrm{d}t. \tag{6}$$

In a similar way, the work performed by the SED device, the energy dissipated by friction and the viscous term are evaluated:

$$w_{\mathrm{SED}} = \int_0^t \frac{F_{\mathrm{SED}}}{M}\dot{X}\mathrm{d}t, \tag{7}$$

$$w_{\mathrm{fric}} = \mu g \int_0^t \mathrm{sgn}\,(\dot{X})\dot{X}\mathrm{d}t = \mu g \int_0^t |\dot{X}|\ \mathrm{d}t, \tag{8}$$

$$w_{\mathrm{vis}} = \frac{C}{M}\int_0^t \dot{X}^2\mathrm{d}t. \tag{9}$$

6. Seismic inputs considered for the evaluation

A method of specifying the seismic hazard level characterizing a specific site is through the corresponding elastic design spectrum. It consists in simple curves indicating the maximum acceleration attained at each natural period. The design spectra contain statistical information of the site seismic activity, the type of soil and the functionality of the addressed building. For the present study, the design spectrum is elaborated in agreement with the Argentinean Seismography Institute INPRES (2013). In the present case, it corresponds to the most hazardous zone with a peak ground acceleration (PGA) up to 4 m s^{-2}, a Type B soil (plate wave velocity from 700 to 1500 m s^{-1}) and a building with the highest functional importance (e.g. a hospital). The spectral content of real earthquake record available from the Peer data base (2016) was modified by means of the software Seism Artif (SEISMOSOFT 2016) to fit them with the selected design spectrum, within a certain tolerance. To account for seismic input variability, five different real earthquake records were adjusted to generate the inputs used for the analysis. The respective time records are presented in figure 8(a) and their spectral distribution compared with the design spectra in figure 8(b). Table 2 summarizes the parameters characterizing the magnitude of each register, i.e., the PGA, velocity PGV and displacement PGD, the Arias intensity AI (Arias 1970) (given by the time integral of the squared acceleration) and

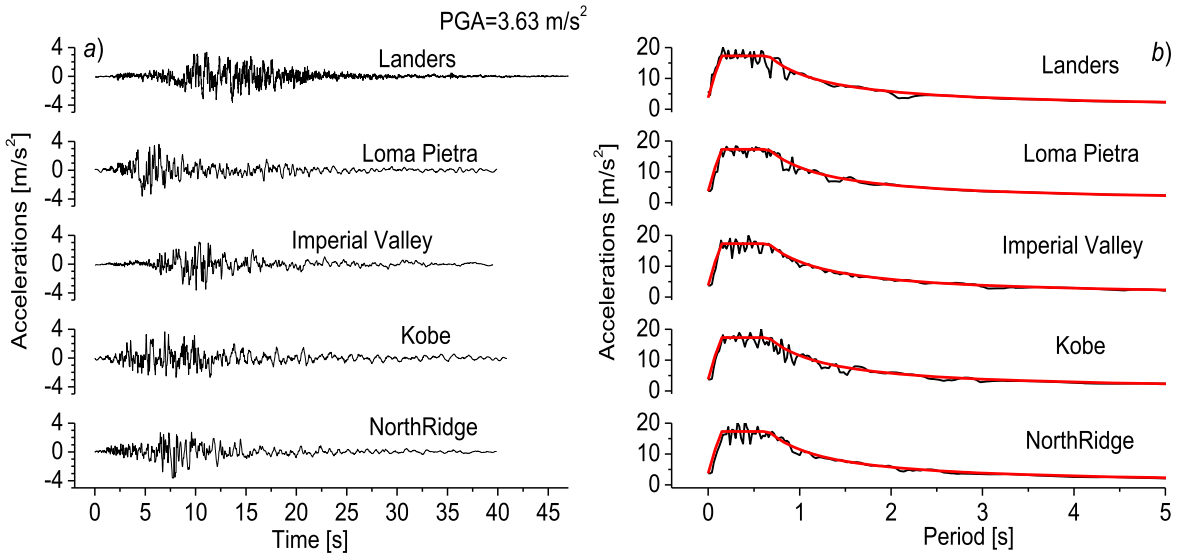

Figure 8. Seismic Ground Shakes inputs used for the analysis. (a) Acceleration registers. (b) Corresponding spectral content of the seismic inputs. Seismic inputs were generated by adapting the original seismic registers to the design spectrum.

Table 2. Summary of seismic inputs used for the study.

	Original data					Modified data				
Input designation	PGA ($m\,s^{-2}$)	PGV ($m\,s^{-1}$)	PGD (m)	AI ($m\,s^{-1}$)	SD (s)	M.PGA ($m\,s^{-2}$)	M.PGV ($m\,s^{-1}$)	M. PGD (m)	AI ($m\,s^{-1}$)	$SD_{5\text{-}95}$ (s)
Northridge	5.58	0.522	0.090	0.028	9.08	3.36	0.899	3.34	0.028	16.02
Kobe	3.38	0.277	0.097	0.018	13.04	3.36	0.778	1.17	0.031	22.16
Loma Pietra	3.60	0.447	0.197	0.014	11.48	3.36	0.974	1.19	0.029	15.67
Imperial Valley	3.09	0.315	0.140	0.005	10.01	3.36	0.661	0.578	0.011	15.74
Landers	7.65	0.321	0.165	0.068	13.76	3.36	0.953	0.374	0.033	11.62

the significant duration SD. In table 2, both the original and the modified values for each of these magnitudes are included. Maximum values corresponding to each column are highlighted in yellow. It can be seen that each of the seismic excitations can be considered as the most demanding, depending on the particular parameter used for qualification.

7. Numerical simulations

Simulations of the dynamic response of the structure were performed for each of the acceleration registers for the different combinations of wire lengths $L = 0.08, 0.16, 0.4, 0.8, 1.6, 3.2, 4$ and 8 m and mass $M = 20, 32, 50, 80, 125, 200, 315, 500, 800, 1260$ and 2000 kg. This totalizes 88 simulations per earthquake. These particular values of the parameters L and M were selected in order to complete an approximately regular point arrange in logarithmic scale in the parametrical space. The simulations were run for times up to 40 s. Equation (5) was integrated numerically following a Newmark type algorithm. The adopted time step was set to 0.001 s but it was reduced each time transition points between elastic and transformational segments or reversion points were reached to get small tolerance displacement values and thus avoiding accumulation of numerical errors. Coefficient C for the viscous damping was set as 1% of the critical viscous damping given by the initial stiffness of the structure. This coefficient was introduced with the aim of improving the stability of the numerical method but, as it will be shown later, it does not exert an important effect on the evaluated responses.

8. Results and discussion

8.1. Dynamic response of the unprotected structure

The resulting displacements and accelerations of the unprotected structure for the five seismic inputs considered are presented in figure 9. Although seismic inputs were adjusted to the same design spectra, Northridge and Loma Pietra results in significant peak displacements which might be related with their near to fault characteristics. Since in the unprotected case the only force transmitted between the ground and the structure is due to friction in the PTFE layer, acceleration of the mass M cannot be higher than that provided by the friction force, i.e. $\mu g \leqslant 0.39\ m\,s^{-2}$. This fact can be appreciated in the graphs of figure 9(b).

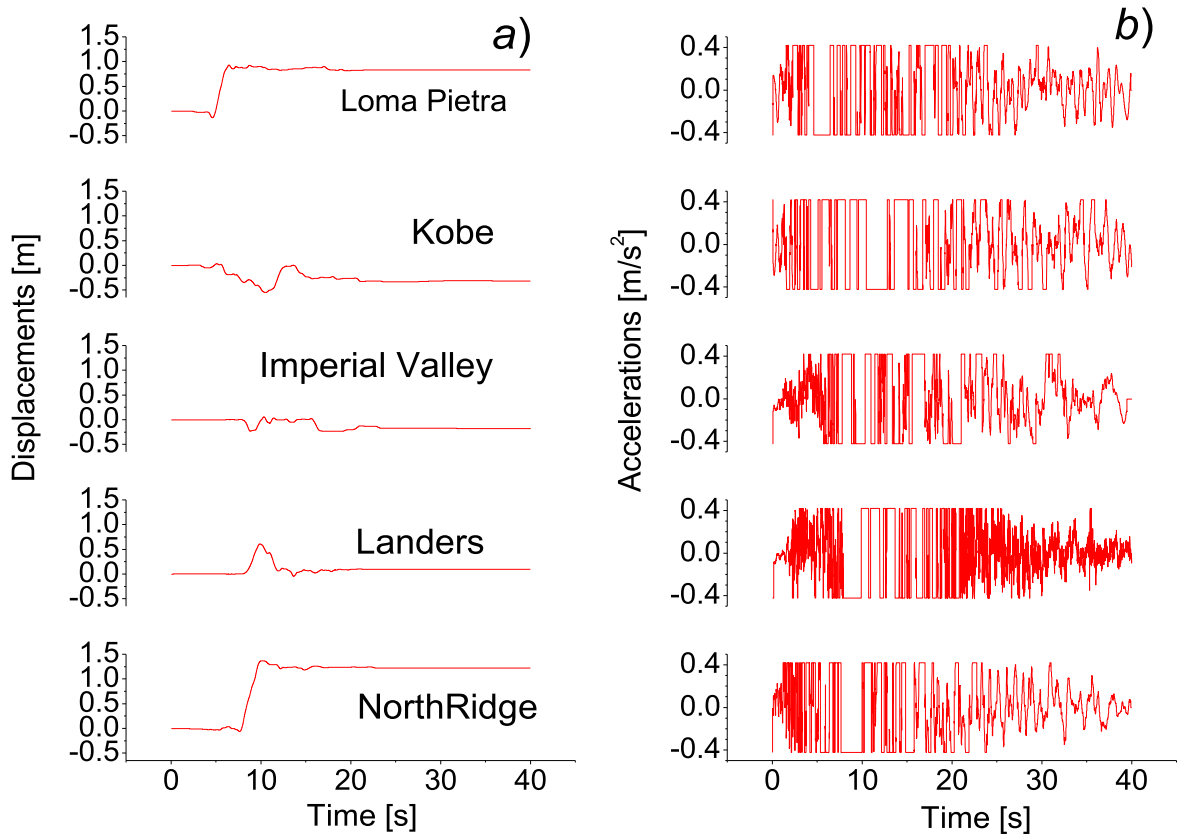

Figure 9. Responses of the unprotected structure to the simulated ground motions: (a) relative displacements between ground and mass *M*. (b) Absolute accelerations of the mass *M*.

8.2. Numerical results for superelastic behavior of type SEB1

In figure 10, contour plots in the space defined by the parameters *L* and *M* corresponding to the response variables selected for evaluating the performance are presented. The values represented were obtained by selecting the highest value among the simulation results for the five earthquakes for each of the *L*–*M* points, i.e., for each of the 88 *L*–*M* combinations, the most demanding result was considered for plotting. As mentioned before, the pairs *L*–*M* selected for simulations spread regularly over the plot in logarithmic scales and the definition of contours is associated with level curves assuming a smooth behavior of the response between neighbor points.

Figure 10(a) corresponds to the mass *M* peak absolute acceleration. In this plot, 40 from the 88 points corresponds to Loma Pietra earthquake, 19 from Northridge, 16 from Imperial Valley, 11 from Landers and 2 from Kobe earthquake. Although Loma Pietra earthquake clearly dominates the most demanding result series, every earthquake can be considered the most hazardous depending on the *L*–*M* combination considered. Considering that the case studied here refers to an isolated structure, maximum peak accelerations exceeding the overall PGA of 3.63 m s^{-2} of the simulated earthquakes (figure 8(a)) would be indicative of a stiffening solution rather than an isolation one. In the plot of figure 10(a), accelerations higher than 8 m s^{-2} were not included with the aim of better resolving values in the range of interest.

Plot in figure 10(b) corresponds to the maximum peak relative displacements of the mass *M* with respect to the ground. In this plot, Loma Pietra contributed with 40 of the 88 points, Northridge 20, Imperial Valley 16, Landers 10 and Kobe 2. The maximum admissible relative displacements values depend on the displacement capacity of the structure bearings, on external requirements as are the presence of neighbor buildings, etc. It is observed that maximum displacement appreciably increases up to 0.7 m in a right upper side portion of the plot. It is precisely in this region where the maximum acceleration exhibits minimum values. This suggests conflicting objectives when simultaneous minimization of both maximum acceleration and maximum displacement are pursued.

In figure 10(c), the maximum strain reached in the NiTi wires is represented. Maximum strains above those values for which fracture would occur constitute unacceptable solutions. A value of 0.08 was adopted to limit the allowed maximum strains in this plot.

With the aim of verifying whether the *L*–*M* domain where the variables plotted in figures 10(a)–(c) exhibit better response correspond to the region in which the SED is effective as a damping device, the ratio between the energy dissipated by the SED and the total input energy is represented in the contour plot of figure 10(d). Where this ratio

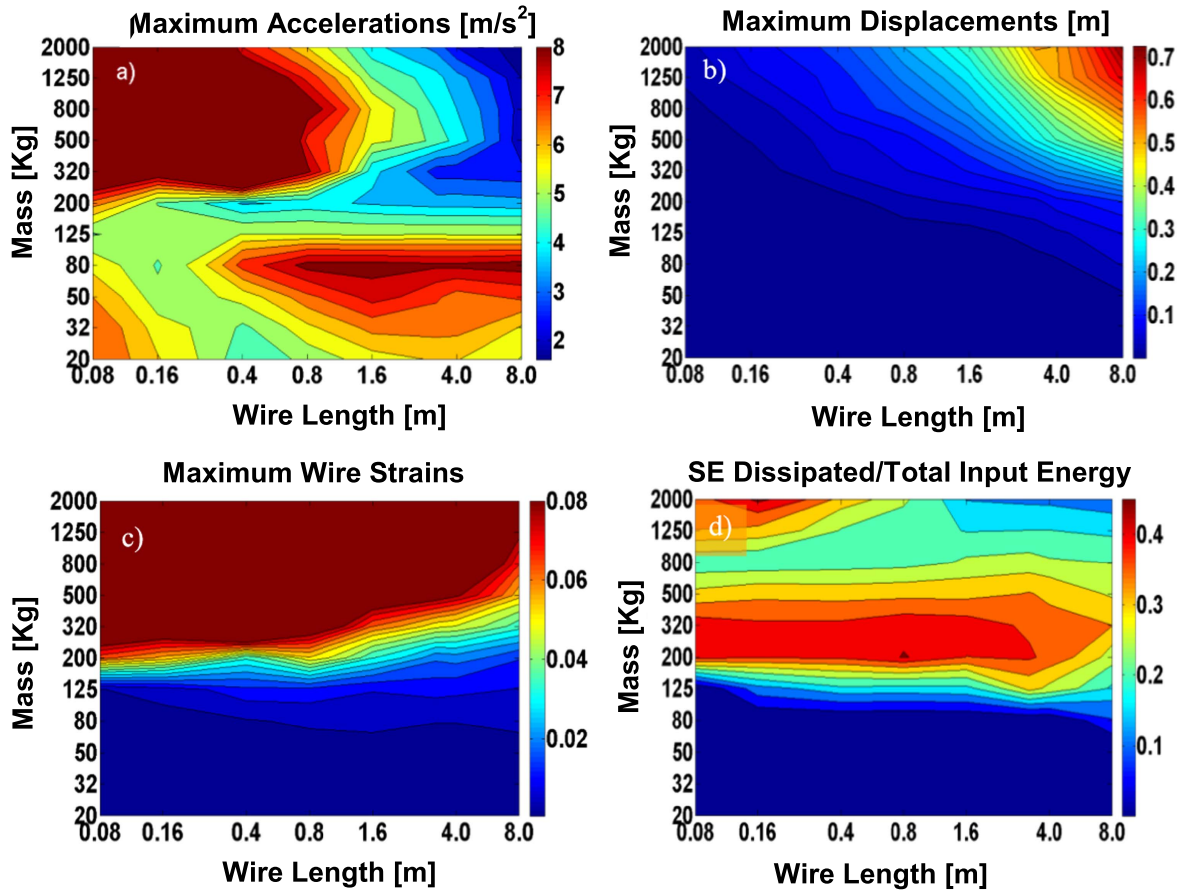

Figure 10. Contour surface plots of results obtained from simulations corresponding to the *L–M* space assuming SEB1. (a) Peak Absolute Accelerations. (b) Maximum relative displacements. (c) Maximum strains in the superelastic wires and (d) ratio between the energy dissipated by superelasticity and the total input energy. The results of each plot correspond to the maximum values obtained among the five simulated earthquake.

drops down to very low values, it means that either the NiTi wires are not strained in the superelastic range or, on the contrary, they are strained to strains exceeding the superelastic maximum strains. In both cases, superelasticity would have negligible influence on the obtained performance.

Therefore, through the type of plots presented in figure 10 it is possible to evaluate the performance of the SED form different perspectives for any *L–M* combination. It is important however to make here some additional considerations. In the maximum strain plot of figure 10(c), a restriction was imposed on this value (8% maximum strain) to avoid fracture of the wires. Although there are no evident restrictions on the maximum accelerations (figure 10(a)) or displacements (figure 10(b)), there may be admissible values stipulated by design codes or by the case specific characteristics. With the aim of going forward with the analysis, an admissible acceleration of 4 m s^{-2} (just above the PGA of 3.63 m s^{-2}) and a maximum displacement of 0.5 m are assumed in the present work. Each one of these three admissible values delimit thus a validity region of the parametric space. The domain from which the competitive configurations should be selected results from the intersection of the mentioned validity regions. In figure 11 the selection domain obtained for the SEB1 case is represented. In this

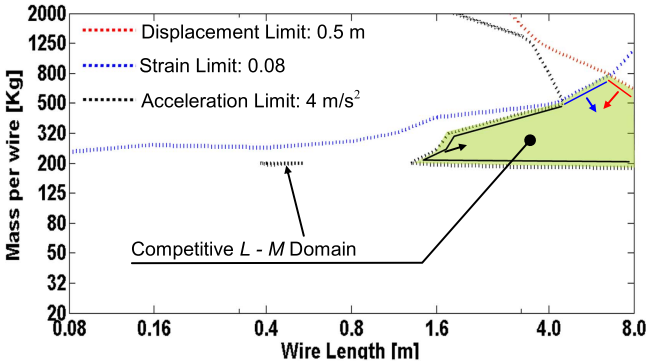

Figure 11. *L–M* domain where SED should be selected for a competitive protection alternative assuming SEB1 behavior.

region, the energy dissipated by SED ranges from 20% to 40% of the total input energy as it can be observed from figure 10(d). This indicates a rather efficient use of the dissipative properties associated with the SED in this *L–M* domain.

In figure 12(a), the results of all the previous simulations are now alternatively plotted in peak acceleration—peak displacement coordinates. Points of the maximum values series are represented by black solid squares. In the same figure the results corresponding to the five earthquakes are

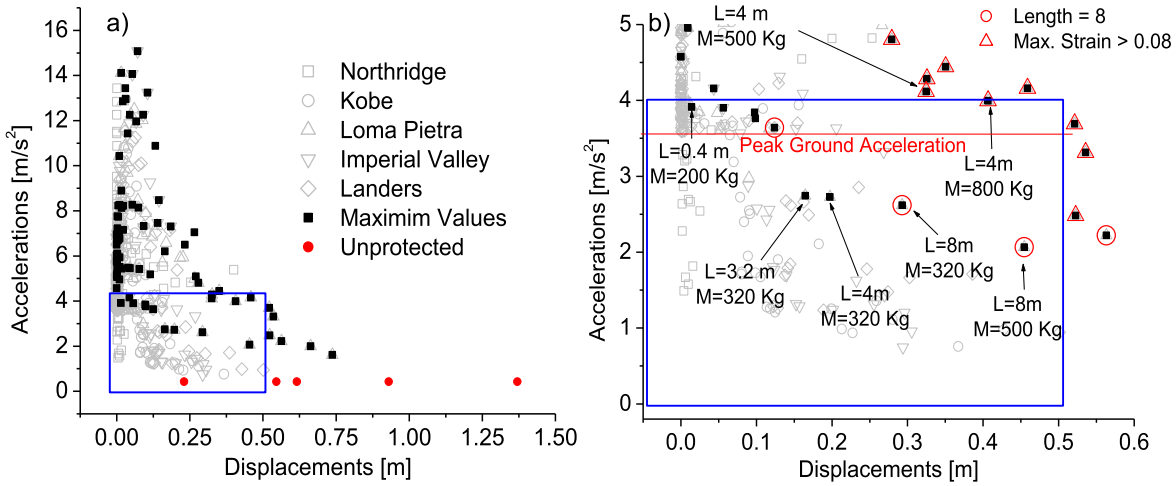

Figure 12. Acceleration and displacements results obtained from simulations assuming SEB1 behavior. (a) Whole set results. (b) Selection box results.

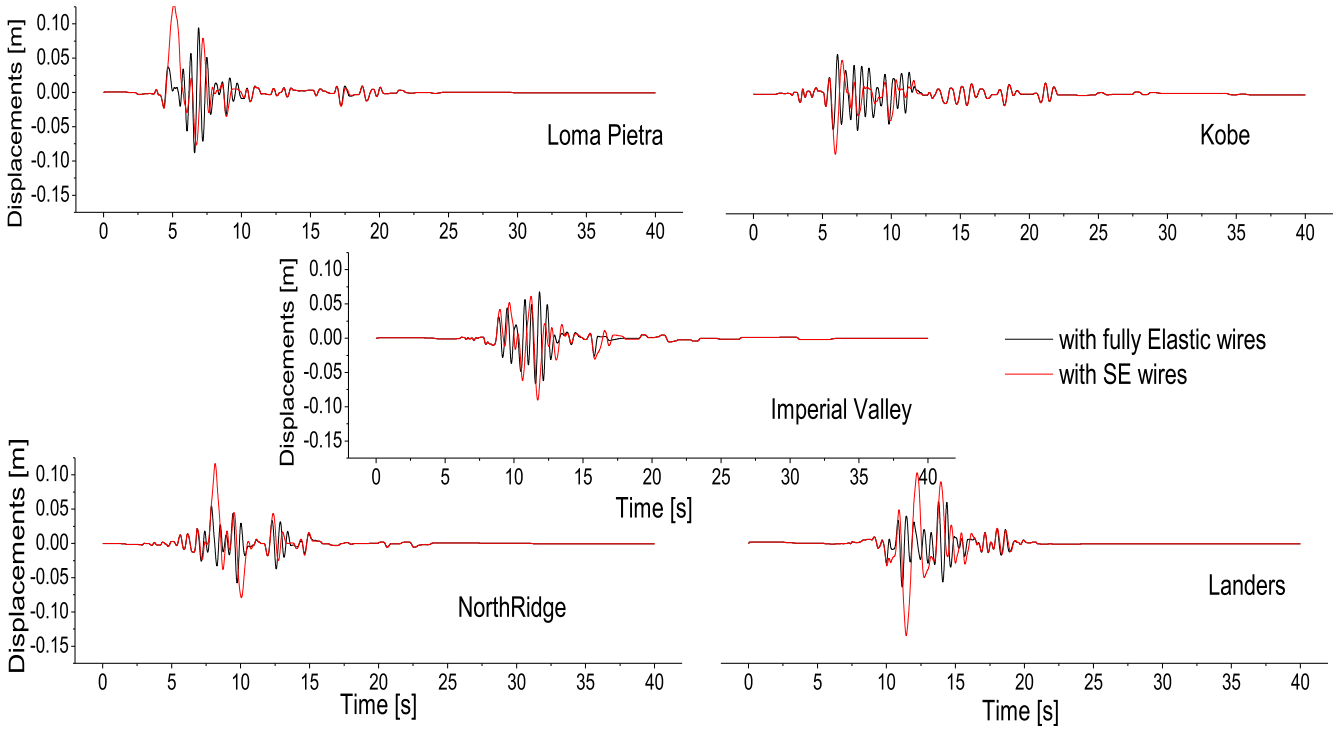

Figure 13. Relative displacement versus time responses obtained assuming SEB1 behavior for the five earthquakes and for a SED with $L = 3$ m and a mass $M = 300$ kg.

represented using light gray open symbols. The width of the cloud constituted by this set gives an insight of the dispersion of the obtained results. Also, in red circles, the results obtained for the unprotected structure were included. This plot allows appreciating at a glance in which magnitude the accelerations and displacements can be modified by the introduction of the SED. Figure 12(b) is a zoom of the selection box included at the lower left of figure 12(a) and bounded by the admissible values of 4 m s^{-2} and 0.5 m. In the cases where the maximum strain exceeds 0.08, the original square solid symbols are distinguished using external red triangles. *L*–*M* parameters are indicated for some of them. Among the valid points lying inside the selection box, the points with 3.2 m–320 kg and 4 m–320 kg are selected as the most competitive configuration for the SED. In a similar manner, the original symbols corresponding to $L = 8$ m are now marked using red circles. They are not ranked however since it is considered that such a high wire length is rather unpractical to be implemented and there are no important improvements that justify their introduction.

Figures 13 and 14 correspond to the displacement versus time and acceleration versus time responses, respectively, obtained for the five earthquakes with parameters of $L = 3$ m and $M = 300$ kg. Responses, in red lines, are compared with those obtained with fully elastic wires with stiffness given by the austenitic elastic modulus E_A, in black lines. On the one hand, it can be seen that the displacement responses show important

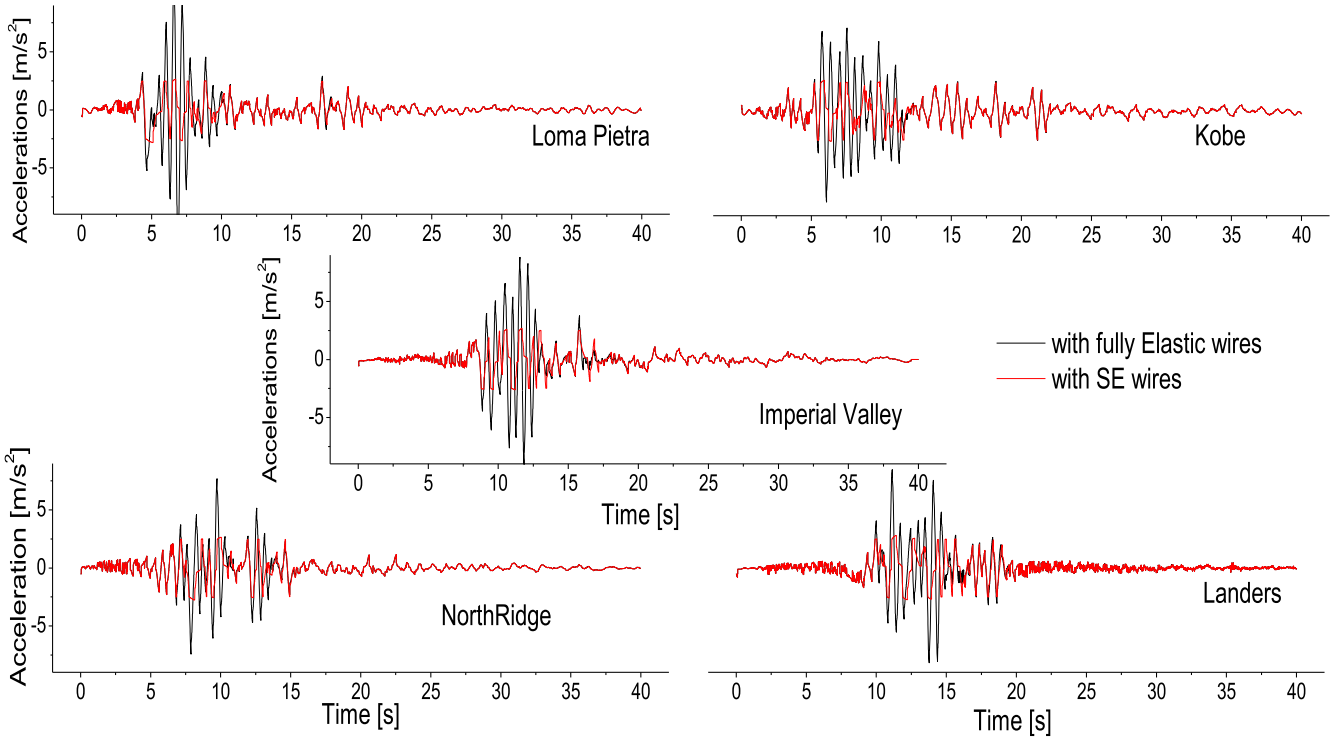

Figure 14. Acceleration versus time responses obtained assuming SEB1 behavior for the five earthquakes and for a SED with $L = 3$ m and a mass $M = 300$ kg.

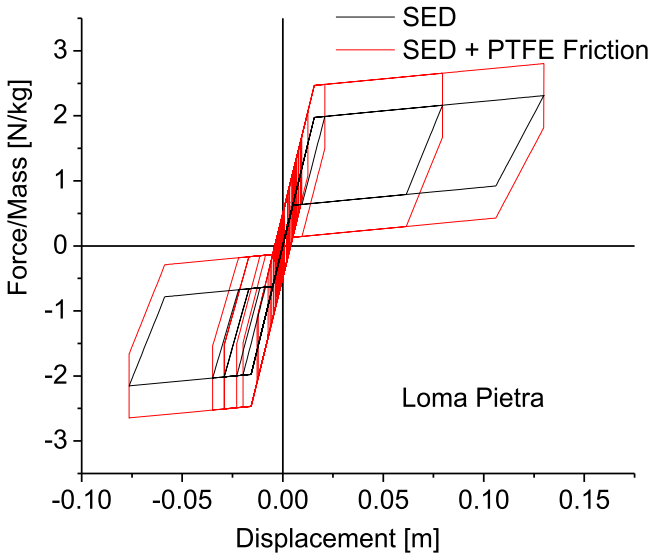

Figure 15. Force/Mass ratio versus displacement response of the structure for the Loma Pietra earthquake assuming SEB1 behavior.

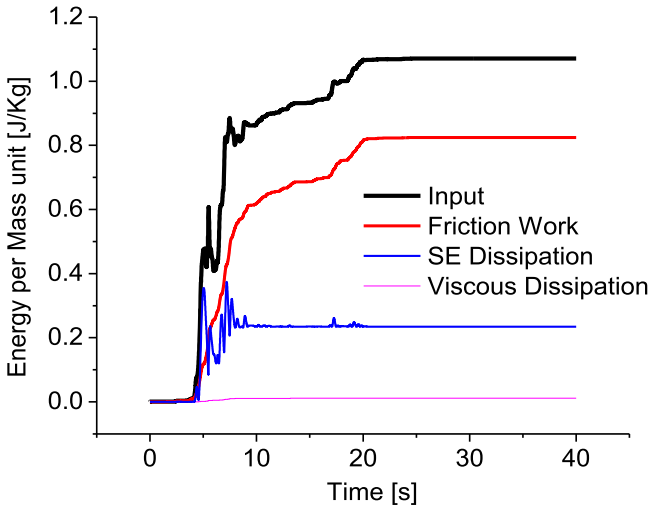

Figure 16. Input and dissipated energy time histories obtained for the Loma Pietra earthquakes for the SEB1 behavior.

reductions respect with the values obtained with the unprotected structures which were shown in figure 9, but do not represent an advantage in comparison with elastic wires with stiffness equivalent to the initial of the SED. On the other hand, accelerations are clearly reduced with respect to fully elastic responses. As it was mentioned above, the aim of reducing acceleration is prioritized in isolation solutions. It can be said that the SED devices is able to restrain maximum displacements keeping accelerations below peak ground values. Another remarkable aspect is that no residual strains are registered at the end of the Earthquakes for both SE and fully elastic wires cases. While the displacement restraining for the fully elastic wires can be related to the stiffening of the structure which also results in rather high accelerations, it is the action of the self-centering forces which plays an important roll upon the recovery of peak displacements when SE wires are used giving place to the mentioned low residual strains.

Figure 15 includes the force-displacement response obtained for the Loma Pietra earthquake. The combined action of the SED plus the PTFE layer friction gives thus the red line response. The presence of the self-centering force due

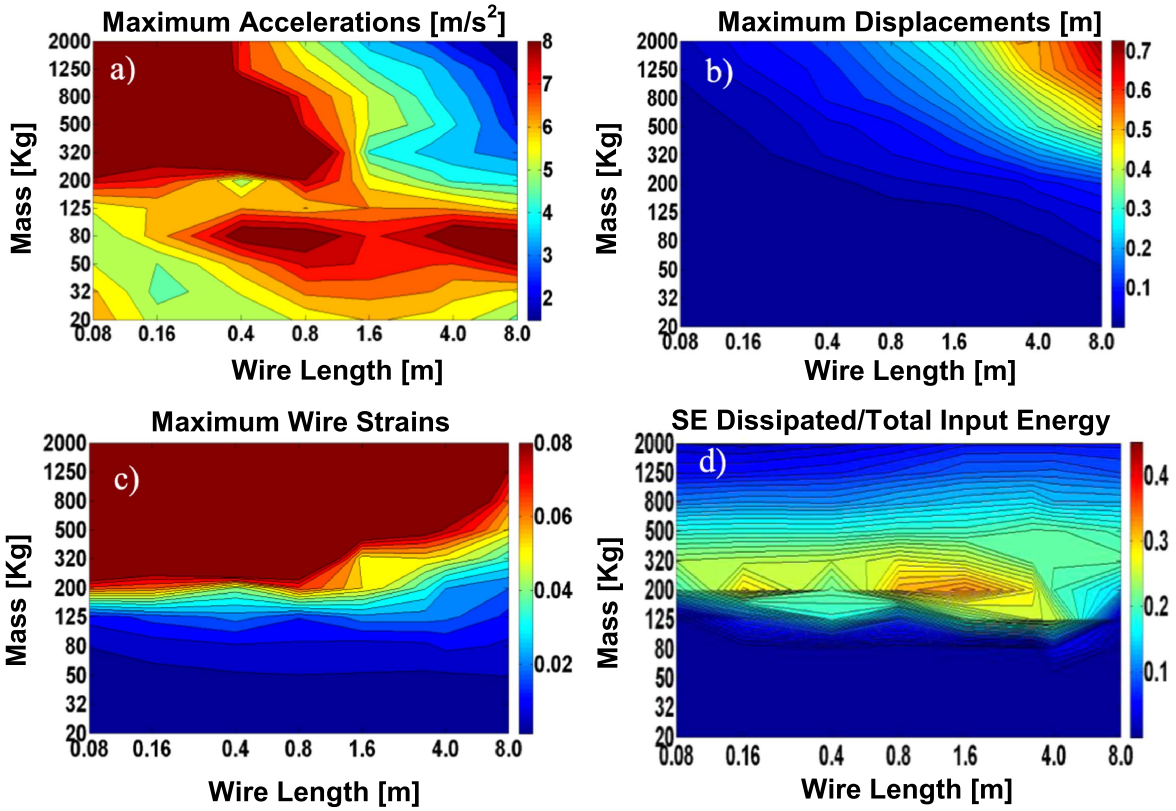

Figure 17. Contour surface plots of results obtained from simulations corresponding to the *L–M* space assuming SEB2. (a) Peak Absolute Accelerations. (b) Maximum relative displacements. (c) Maximum strains in the superelastic wires and (d) ratio between the energy dissipated by superelasticity and the total input energy. The results of each plot correspond to the maximum values obtained among the five simulated earthquake.

superelasticity up to near zero displacement is here again clearly evidenced. In figure 16 the accumulated inputed and dissipated energy for all the actuating mechanism are represented in terms of the fraction with respect to the total work input. Although the main contribution to the dissipation is made by the PTFE layer, SED dissipated energy fraction reaches values close to 40%. The energy dissipated by the assumed viscous damping resulted insignificant in relation to the others mechanisms, concluding that its introduction does not play a relevant roll in the obtained responses.

8.3. Numerical results for superelastic behavior of type SEB2

The same analysis performed in the previous section is repeated for the SEB2 superelasic behavior characterized by a smaller stress hysteresis width and higher critical stress and transformational slope. Construction of the contour plots of figure 17 was made following the same criteria described before for the different contours included in figure 10. In this case, Loma Pietra earthquakes presents highest accelerations for 49 parameters combinations, Northridge for 19, Imperial Valley for 12, Landers for 5 and Kobe for 3. Regarding accelerations, Loma Pietra resulted in the most demanding earthquake also in 49 combinations, Northridge in 17, Imperial Valley in 12, Landers in 7 and Kobe in 3. Again, the

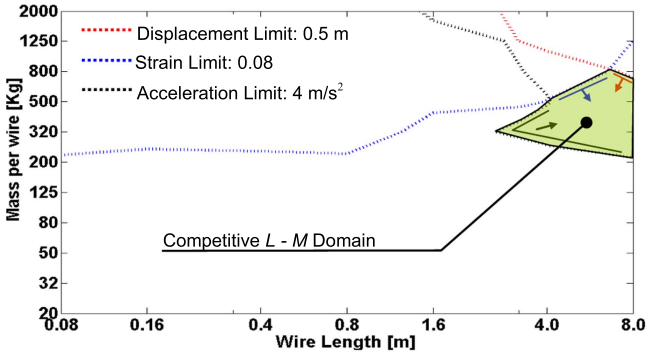

Figure 18. *L–M* domain where SED should be selected for a competitive protection alternative assuming SEB2 behavior.

Loma Pietra seems to be the most hazardous earthquake but not for the totality of the *L–M* combinations.

The resultant contour plots present similarities with those obtained assuming the SEB1 behavior. Assuming again the admissible values of strains, accelerations and displacements in 0.08, 4 $m\,s^{-2}$ and 0.5, respectively, the corresponding selection domain is now presented in figure 18. Its extension is clearly smaller compared with the obtained for SEB1 (figure 11). In this domain, the energy dissipated by the SED assuming SEB2 behavior reaches around 20% of the total input energy as it can be observed from figure 17(d).

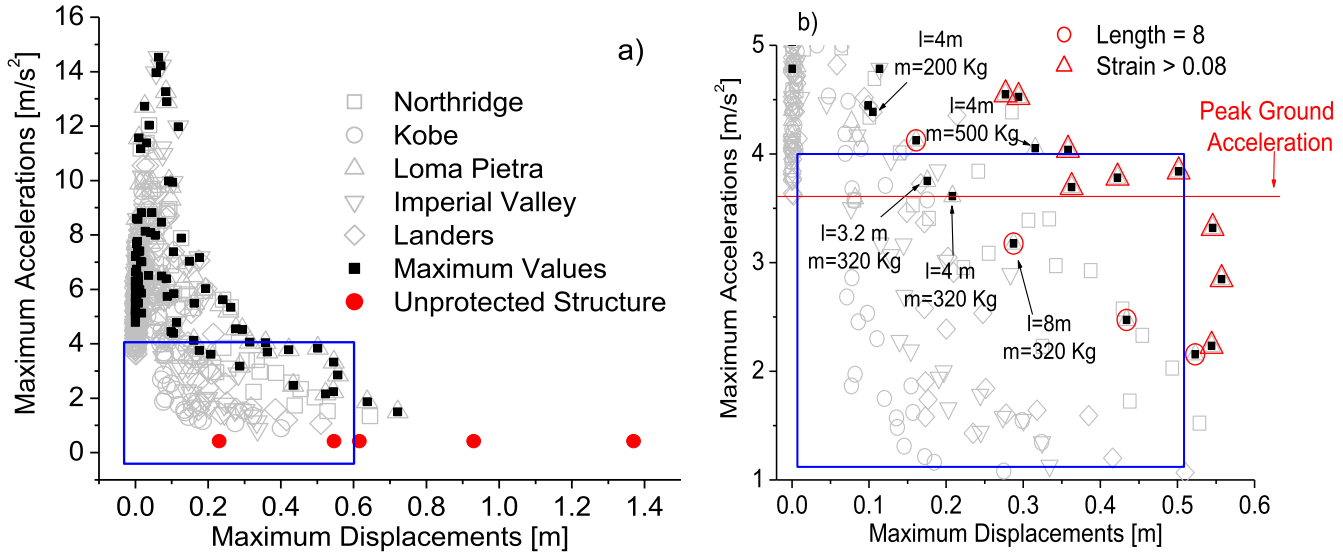

Figure 19. Maximum absolute accelerations versus maximum relative displacements obtained during the simulations, considering SEB2 behavior (a) whole range of results, (b) details of results included into the selection region. Coordinates of black square points correspond to the most demanding results among the five earthquakes for each parameter pair.

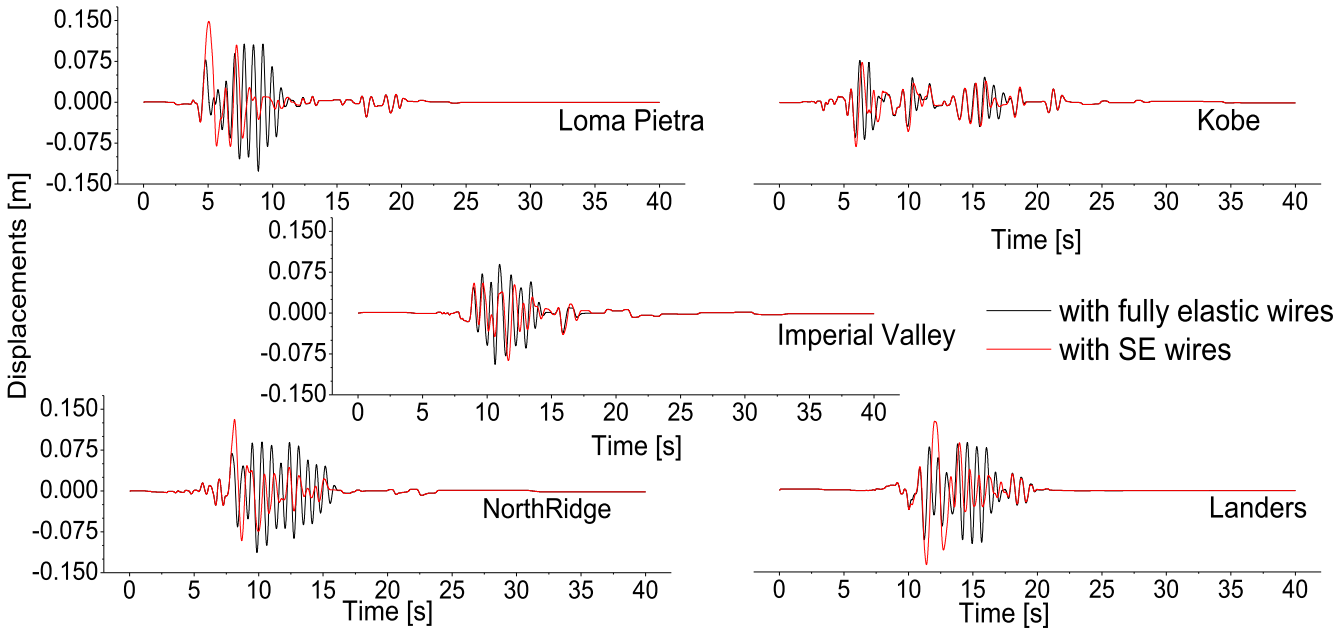

Figure 20. Relative displacement versus time responses obtained assuming SEB2 behavior for the five earthquakes and for a SED with $L = 3$ m and a mass $M = 300$ kg.

Figure 19 corresponding to the SEB2 behavior is the equivalent of figure 12 for SEB1. Figure 19(a) includes the whole set of results in light gray open symbols. Filled black squares symbols correspond to the highest acceleration–highest displacement pair among the five earthquakes and red circles are results of the unprotected structure. Figure 19(b) shows in detail the selection box limited by maximum accelerations of 4 m s^{-2} and maximum displacements of 0.5 m. There are 7 of the 88 points lying inside the box. Three of these points, the ones surrounded by an open red triangle, must be discarded because they have associated maximum strains higher than 0.08. Additionally, the two points surrounded by open circles are not ranked because they correspond to 8 m wires, considered of impractical implementation. Finally, only 2 of the 7 points inside the selection box are admissible, being them coincident with the ones selected in figure 12 (combination of 3.2 m/320 kg and 4 m/320 kg). The location of the $L = 8$ m/$M = 320$ kg point suggest that lengths higher than 4 m would give smaller peak accelerations.

Figure 20 includes the displacement versus time responses and figure 21 the accelerations versus time responses of the five earthquakes evaluated with parameters $L = 3$ m and $M = 300$ kg; i.e., the same parameters used for the simulations in figures 13 and 14 assuming SEB1. As in those figures, the responses are compared with the obtained with fully elastic wires with stiffness equivalent to the initial

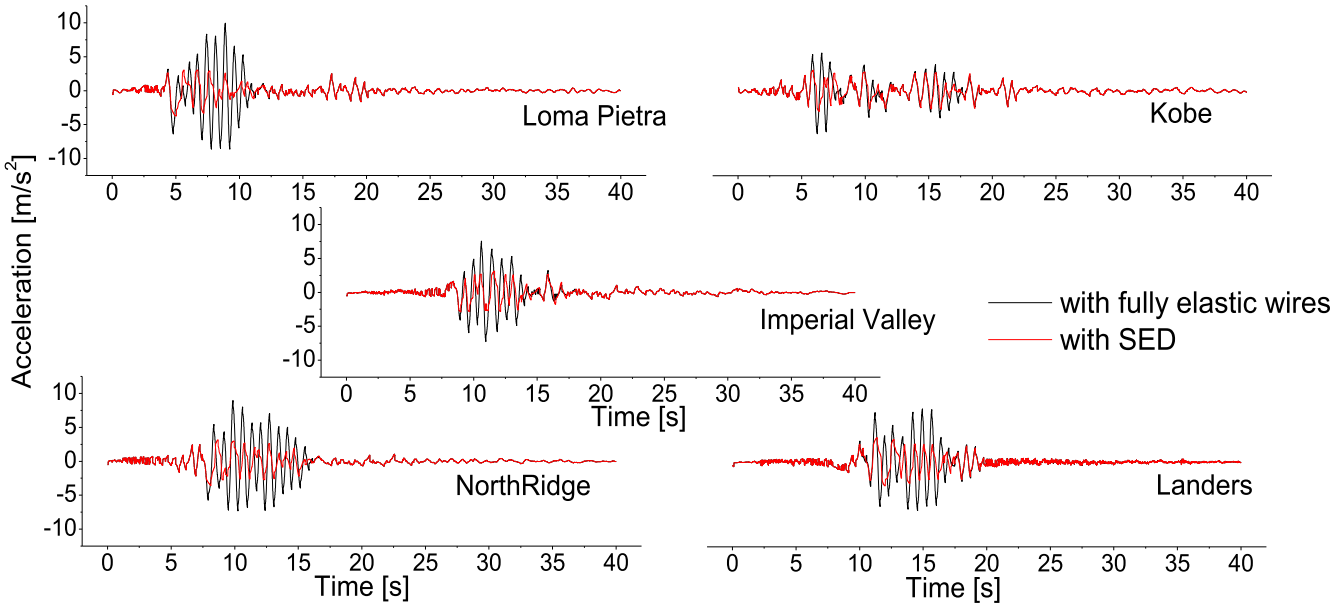

Figure 21. Acceleration versus time responses obtained assuming SEB2 behavior for the five earthquakes and for a SED with $L = 3$ m and a mass $M = 300$ kg.

of the SED. Maximum displacements are reduced in all cases respect to those corresponding to the unprotected structure, but not if they are compared with the fully elastic system responses. Regarding absolute accelerations, even though the peak values obtained with the SED are not reduced as much as in the case of the unprotected structure, there is a clear improvement respect the structured equipped only with fully elastic devices. An important result is that, in any case, appreciable residuals displacements are registered after the Earthquakes. Figure 22 corresponds to the *F*–*X* response of the Loma Pietra earthquake. There is a clear smaller relative weight in the hysteresis area represented by the superelastic cycles respect to the total area in comparison with figure 15 corresponding to SEB1. This fact is also reflected in figure 23, where input work and dissipated energy flows were represented normalized with the total input work at the end of the Earthquake. The energy dissipated by the SED device represents less than 20% of the total input work. As it was the case in figure 16, the energy dissipated by viscous damping is very low with respect to the energy dissipated by superelasticity and friction.

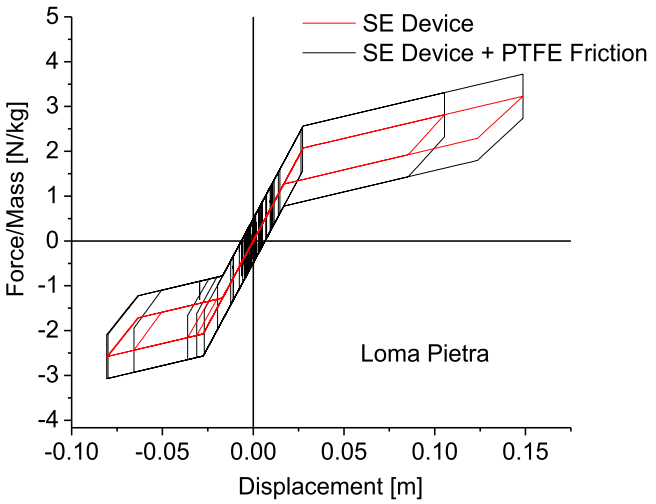

Figure 22. Force/Mass ratio versus displacement response of the structure for the Loma Pietra earthquake assuming SEB2 behavior.

9. Further remarks

The study carried out in the present work indicates the convenience of including as many earthquakes in the analysis as it is possible to have a wide coverage of the highly variable nature of seismic inputs. It could be seen that even though the five accelerograms were adjusted to fit a single design spectrum, the responses of the unprotected structure exhibited important differences. In particular, Loma Pietra and Northridge registers cause notably higher peak and residual displacements than the rest, being the most hazardous. Concerning the responses of the protected structure, it depends upon the SED configuration which earthquake originates the highest peak displacement or peak accelerations. Therefore, a conservative criterion for the construction of contour plots and for selecting the most convenient parameter combination was considered. This was done by extracting, for each SED configuration, maximum peak values among the five earthquakes that have been considered.

The contour plots and peak acceleration versus peak displacements graphs give an insight about performance levels that can be accomplished over a bi-dimensional space generated by length L and mass M ranges extended beyond the practicable values in the case of wire length. Through this whole response picture, it can be concluded about the

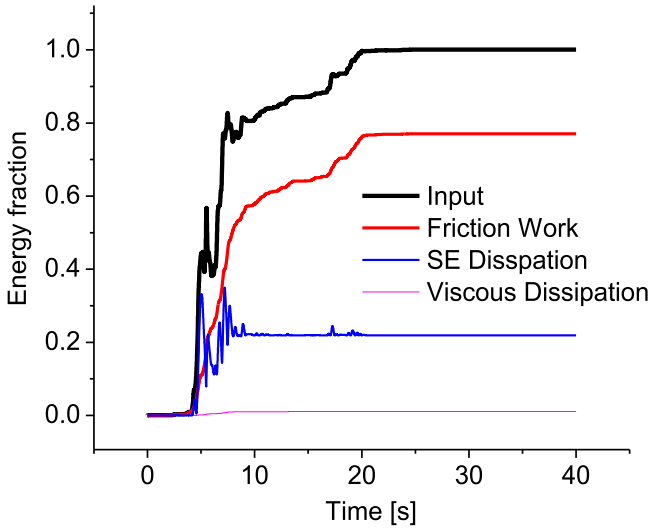

Figure 23. Input and dissipated energy time histories during the Loma Pietra earthquake assuming SEB2 behavior.

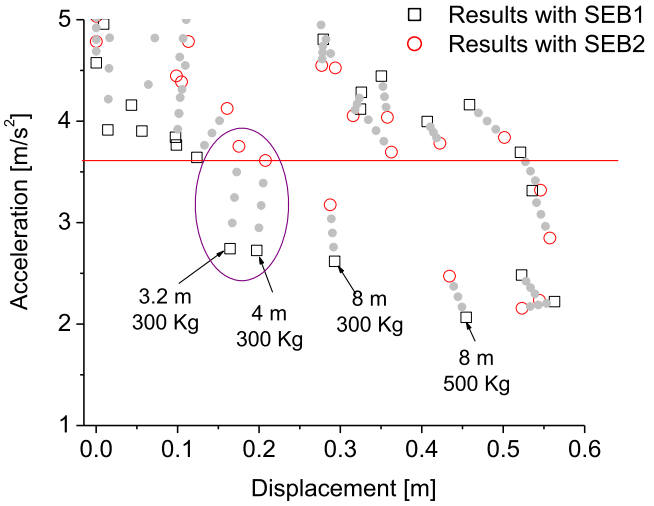

Figure 24. Comparison of results obtained with SEB1 and SEB2 superelastic behaviors.

suitability of this protective strategy and the most convenient device configurations for a seismicity level given by the site characteristic. In this work, the selection region is defined as that for which peak displacements and acceleration are simultaneously diminished but prioritizing the last since this is an intended isolated structure. This analysis methodology can be easily adapted to other problems involving different structural systems, objective variables and configuration parameters.

An aspect of the analysis to be further discussed refers to the simplicity of the adopted models for the description of the dynamics of the structure (1 DOF) as well as for the superelastic material behavior (independent of temperature and strain rate). 1 DOF assumption is usually implemented in first approaches for the sake of simplicity and it turns more realistic in the case of very soft first deformation mode as it occurs in an isolated structure. The frequency dependence of the force versus displacement superelastic behavior (Soul and Yawny 2013) is not reproduced by the adopted behavior model for the sake of computing economy. Instead, the numerical analysis is repeated for two fixed material behavior named SEB1 and SEB2, corresponding to the lowest (0.001 Hz) and highest (5 Hz) tested frequency condition. Since these two material behaviors were taken from low and high extreme frequencies, a reasonable assumption is that real values would fall somewhere between the two calculated solutions. A graph merging plots of figures 12(b) and 19(b) is included in figure 24 form where it is possible to compare results obtained assuming SEB1 and SEB2. The magnitude of differences between SEB1 and SEB2 results depends upon the considered configuration, being relatively important for example for L/M values of 3.2 m/300 kg. This fact seems to justify efforts for implementing superelastic models able to reproduce frequency or strain rate dependence to improve the predictably of the analysis. However, results obtained in this study allow concluding that most convenient SED configuration should be inside the region around the selected points 3.2 m–300 Kg and 4 m–300 Kg.

10. Conclusions

The parametric analysis carried out allowed for a complete assessment of the dynamical responses attainable by an isolated structure protected with a SED, for ground shake inputs compatible with the highest seismicity zone of the Argentinean zone map.

It is observed that most the convenient SED configurations, for which both peak absolute accelerations and relative displacements are diminished lie around the region of 3.2–4 m of wire length and 300 kg of associated mass. The conservative criterion adopted assures that the peak accelerations can be kept below the PGA of 3.6 m s^{-2} (or slightly above in the worst case, assuming the SEB2 material behavior) and displacement below 0.25 m, also accomplishing the restriction of wire strains smaller than 0.08. Also, no residual displacements would remain after the seismic actions.

These results allow concluding that the studied device is suitable for seismic protection of isolated structures. Also, simulations show that the SED contribution to the dissipated energy is between 20 and 40% of the total input energy, i.e., most of the energy is dissipated by friction. Therefore, it can be argued that the protective action of the SED is more associated with its restraining and self-centering properties rather than with its damping capacity.

With the SED configuration already defined, further analysis can be carried out to predict more accurately dynamical responses. Complex models for structural elements and material can be then implemented. Also, the lengths and masses values here considered can help to project suitable facilities for experimental assessment of this type of protective systems based on the superelastic behavior exhibited by shape memory alloys.

Acknowledgments

Authors acknowledge CONICET, CNEA and UNCuyo for financial support.

References

Arias A 1970 *A Measure of Earthquake Intensity in Seismic Design for Nuclear Power Plants* ed R J Hansen (Cambridge, MA: MIT Press) pp 438–83

Attanasi G and Auricchio F 2011 Innovative superelastic isolation device *J. Earthquake Eng.* **15** 72–89

Attanasi G, Auricchio F and Fenve G 2009 Feasibility assessment of an innovative isolation bearing system with shape memory alloys *J. Earthq. Eng.* **13** 18–39

Biritignolo M, Bonci A and Viskovic A 2000 Numerical models for masonry façade walls with and without SMADs *Proc. Final Workshop of the ISTECH Project-Shape Memory Alloys Devices for Seismic Protection of Cultural Heritage Structures* (Ispra, Italy: Joint Research Centre) pp 117–40

Cardone D 2012 Re-centering capability of flag-shaped seismic isolation systems *Bull. Earthq. Eng.* **10** 1267–84

Casciati S, Faravelli L and Hamdaoui K 2007 Performance of a base isolator with shape memory alloy bars *Earthq. Eng. Eng. Vib.* **6** 401–8

Casciati S, Faravelli L and Vecce M 2017 Investigation on the fatigue performance of Ni–Ti thin wires *Struct. Control Health Monit.* **24** e1855

Chen Y, Jiang H C, Liua S W, Ronga L J and Zhao X Q 2009 The effect of Mo additions to high damping Ti–Ni–Nb shape memory alloys *Mater. Sci. Eng.* A **512** 23–31

Chopra A K 1985 *Dynamics of Structures* (Englewood Cliffs, NJ: Prentice-Hall)

Dell Ville R, Malard B, Pilch J, Sittner P and Schryvers D 2010 Microstructure changes during non-conventional heat treatment of thin Ni–Ti wires by pulsed electric current studied by transmission electron microscopy *Acta Mater.* **58** 4503–15

DesRoches R and Delemond M 2002 Seismic retrofit of simply supported bridges using shape memory alloys *Eng. Struct.* **24** 325–32

Dolce M and Cardone D 2005 Fatigue resistance of SMA-martensite bars subjected to flexural bending *Int. J. Mech. Sci.* **47** 1693–717

Erot M 2007 Advanced models for sliding seismic isolation and applications for typical multi-span highway bridges *PhD Thesis* Georgia Institute of Technology

Gao G, Jeon J, Hodgson D and DesRoches D 2016 An innovative seismic bracing system based on a superelastic shape memory alloy ring *Smart Mater. Struct.* **25** 055030

Graesser E and Cozzarelli F 1991 Shape-memory alloys as new materials for aseismic isolation *J. Eng. Mech.* **117** 2590–608

Han Y, Xing D, Xiao E and Li A 2005 NiTi-wire shape memory alloy dampers to simultaneously damp tension compression and Torsion *J. Vib. Control* **11** 1067–84

INPRES 2013 Reglamento Argentino para Construcciones Sismorresistentes-Parte I, Construcciones en General-Julio de 2013-Instituto Nacional de Prevención Sísmica

Kelly T 2001 *Base Isolation of Structures: Design Guidelines* (Wellington, New Zealand: Holmes Consulting Group)

Launey M, Robertson S, Vien L, Senthilnathan K, Chintapalli P and Pelton A 2014 Influence of microstructural purity on the bending fatigue behavior of VAR-melted superelastic Nitinol *J. Mech. Behav. Biomed. Mater.* **34** 181–6

Ling Y and Ling H 2012 Parameters analysis of Re-centring SMA damper based on SAP2000 *Appl. Mech. Mater.* **166–169** 219–25

Masuda A and Noori M 2002 Optimization of hysteretic characteristics of damping devices based on pseudoelastic shape memory alloys *Int. J. Non-Linear Mech.* **37** 1375–86

Mirzaeifar R, DesRoches R and Yavari A 2010 Exact solutions for pure torsion of shape memory alloy circular bars *Mech. Mater.* **42** 797–806

Miyazaki S, Otsuka K and Suzuki Y 1981 Transformation pseudoelasticity and deformation behavior in a Ti-50.6 at% Ni alloy *Scripta Metall.* **15** 287–92

Otsuka K and Wayman C 1998 *Shape Memory Materials* (Cambridge: Cambridge University Press)

Ozbulut O, Hurlebaus S and Desroches R 2011 Seismic response control using shape memory alloys: a review *J. Intell. Mater. Struct.* **22** 1531–49

Ozbulut O and Silwal B 2016 Performance assessment of buildings isolated with S-FBI system under near-fault earthquakes *J. Smart Struct. Syst.* **17**

PEER 2000 Pacific Earthquake Engineering Research Strong Motion Database (http://peer.berkeley.edu/smcat)

Reedlunn B, Daly S and Shaw J A 2013 Superelastic shape memory alloy cables: Part I – isothermal tension experiments *Int. J. Solids Struct.* **50** 3009–26

Saadat S, Salichs J, Noori M, Hou Z, Davoodi H, Baron I, Suzuki Y and Masuda A 2002 An overview of vibration and seismic applications of NiTi shape memory alloy *Smart Mater. Struct.* **11** 218–29

SEISMOSOFT 2016 www.seismosoft.com

Soul H and Yawny A 2013 Thermomechanical model for evaluation of the superelastic response of NiTi shape memory alloys under dynamic conditions *Smart Mater. Struct.* **22** 035017

Soul H and Yawny A 2015 Self-centering and damping capabilities of a tension-compression device equipped with superelastic NiTi wires *Smart Mater. Struct.* **24** 075005

Speicher M, Hodgson D, DesRoches R and Leon R 2009 Shape memory alloy tension/compression device for seismic retrofit of buildings *J. Mater. Eng. Perform.* **18** 746–53

Tanaka Y, Himuro Y, Kainuma R, Sutou Y, Omori T and Ishida K 2010 Ferrous polycrystalline shape-memory alloy showing huge superelasticity *Science* **327** 1488–90

Terriault P, Torra V, Fischer C, Brailovski V and Isalgue A 2007 Superelastic shape memory alloy damper equipped with a passive adaptative prestraining mechanism *Proc. Ninth Canadian Conf. Earthquake Engineering (Ontario, Canada, 26–29 June 2007)* pp 1489–96

Torra V, Casciati S and Vece M 2017 Shape memory alloys wires: from small to medium diameter *Adv. Sci. Technol.* **101** 79–88

Torra V, Isalgue A, Auguet C, Carreras G, Lovey F, Soul H and Terriault P 2009 Damping in civil engineering using SMA. The fatigue behavior and stability of CuAlBe and NiTi alloys *J. Mat. Eng. Perform.* **18** 738–45

Torra V, Martorell F, Sun Q, Ahadi A, Lovey F and Sade M 2016 Metastable effects on martensitic transformation in SMAs Part X. An approach to thermodynamic changes induced for the S-shaped cycles in thick wires of NiTi *J. Therm. Anal. Calorim.* **1** 259–70

Ulmer J, Nusskern H and Sedlmayr G 2015 Influence of pre-strain and thermo-mechanical treatment of next generation nitinol materials in rotary-bending fatigue *Int. Conf. on Shape Memory and Superelastic Technologies (SMST)* 18–22 May 2015(ASM) pp 37–8

Wilson J, Eeri M and Wesolowskya M 2005 Shape memory alloys for seismic response modification: a state-of-the-art review *Earthq. Spectra* **21** 569–601